

Improved Synthesis of Aligned Arrays of Single-Walled Carbon Nanotubes and Their Implementation in Thin Film Type Transistors[†]

Coskun Kocabas,^{‡,§,¶,||} Seong Jun Kang,^{§,¶,‡} Taner Ozel,[‡] Moonsub Shim,^{§,¶,||} and John A. Rogers^{*,§,||,⊥,+,#}

Department of Physics, Department of Materials Science and Engineering, Department of Mechanical Science and Engineering, Department of Electrical and Computer Engineering, Department of Chemistry, Beckman Institute for Advanced Science and Technology, Frederick Seitz Materials Research Laboratory at the University of Illinois, Urbana-Champaign, Illinois, and Division of Advanced Technology, Korea Research Institute of Standards and Science, Daejeon, 305-340 South Korea

Received: February 18, 2007; In Final Form: July 6, 2007

We report optimized chemical vapor deposition growth procedures that can produce arrays of individual single walled carbon nanotubes (SWNTs) in horizontal configurations with perfect linear shapes to within experimental uncertainties and with levels of alignment >99.9%. This process also enables simultaneous growth of random networks of SWNTs integrated with the arrays in complex layouts. The electrical properties of thin film type transistors formed with SWNTs grown in this fashion approach expectations based on the intrinsic properties of the pristine, individual SWNTs. The procedures described here might represent a strategy to large scale integration of SWNTs into devices for applications in electronics and optoelectronics, sensing, nanomechanical systems, and other areas.

Benchmarking studies of the transport properties of semi-conducting single-walled carbon nanotubes (SWNTs) indicate certain important advantages compared to single-crystal silicon in both bulk wafer and nanowire structural forms.^{1–3} These findings together with promising demonstrations of SWNTs as active elements in sensors,^{4–6} optoelectronic devices,⁷ transparent conductors,⁸ and thin film electronics^{9–12} create interest in the development of scalable means for integrating SWNTs into devices, circuits, and systems.^{13–21} One strategy involves the formation of effective conducting or semiconducting thin films that consist of random networks^{9,22} or well-aligned arrays of SWNTs.^{23–26} The large number of SWNTs that are active in devices (e.g., transistors) formed with such “films” enables high-current outputs with statistical averaging effects that provide good device-to-device uniformity in properties even with SWNTs that are electronically heterogeneous.¹⁷ The aligned arrays have advantages compared to the random networks because they avoid percolation transport pathways,^{11,12,27} unusual scaling of device properties,²⁸ tube/tube junction resistances, and other features that might be undesirable for many applications.²⁹ Achieving the ideal configuration of perfectly aligned horizontal arrays of perfectly linear SWNTs at high but submonolayer densities, as measured by the number of SWNTs

per micron, represents a significant experimental challenge. Nevertheless, methods that use guided chemical vapor deposition (CVD) growth of SWNTs on certain types of single-crystal substrates^{22–26} appear promising, particularly when implemented with strategically designed patterns of catalyst.²⁴ This paper presents a range of results on SWNT arrays formed using optimized implementations of procedures of this type, as well as the electrical and scaling properties of thin film transistor devices that are constructed with them. The extremely high quality of the arrays, the ease with which they can be integrated into devices, and the excellent performance that can be achieved suggest that these approaches have the potential to provide a realistic pathway to SWNT-based electronics and optoelectronics, sensors, and other systems.

For growth of the arrays, we start with recently reported procedures that use CVD of SWNTs on thermally annealed quartz substrates. The basic alignment mechanism in this system is thought to involve preferential growth along step edges³⁰ and/or along certain crystallographic directions due to orientationally anisotropic interaction energies between the tubes and the quartz.²⁶ When the catalyst is uniformly distributed on the substrate at moderately low densities (i.e., ~ 10 particles/ μm^2), the growth can yield extremely linear, well-aligned and long tubes but at low densities (~ 0.2 SWNT/ μm).²³ Many applications, however, demand much higher densities, preferably approaching a full monolayer. (Multilayer arrangements can frustrate field effect current modulation in thin film transistors.) Increasing the catalyst density increases the tube density but with reductions in the average tube length, degree of alignment, and linearity in the shape.²⁴ These effects are thought to be due to unwanted interactions between unreacted catalyst particles and growing SWNTs. Patterning the catalyst into strategic locations (e.g., stripes oriented perpendicular to the preferred growth direction) avoids this problem and provides a means

[†] Part of the special issue “Richard E. Smalley Memorial Issue”.

* To whom correspondence should be addressed. E-mail: jrogers@uiuc.edu.

[‡] Department of Physics, University of Illinois.

[§] Department of Materials Science and Engineering, University of Illinois.

^{||} Department of Mechanical Science and Engineering, University of Illinois.

[⊥] Department of Electrical and Computer Engineering, University of Illinois.

⁺ Department of Chemistry, University of Illinois.

[#] Beckman Institute for Advanced Science and Technology, University of Illinois.

[¶] Frederick Seitz Materials Research Laboratory at the University of Illinois.

[‡] Korea Research Institute of Standards and Science.

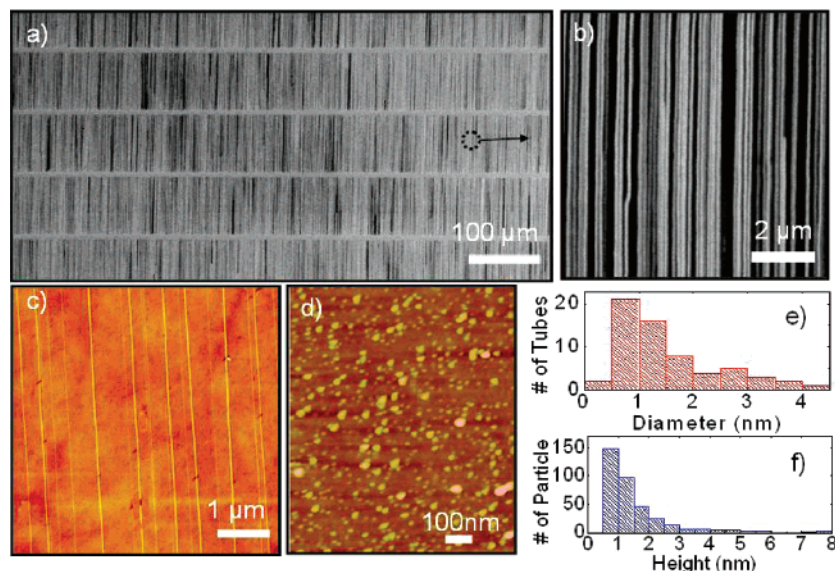


Figure 1. (a, b) SEM images of aligned SWNT arrays collected at different magnifications. The tube density is ~ 5 SWNT/ μm . The bright horizontal lines in (a) correspond to random networks of SWNT that form near the Fe catalyst that exists in these locations. (c) AFM images of selected SWNTs in these arrays. (d) AFM images of iron oxide catalyst particles after 1.5 h annealing process. Distribution of diameters of SWNTs in the arrays (e), and catalyst particles (f) measured by AFM. The average diameter is ~ 1.2 nm for SWNTs and ~ 1.8 nm for the catalyst particles.

for increasing the SWNT coverage while maintaining the alignment, length, and linear geometries.²⁴

This paper introduces important improvements in this basic approach, including optimized annealing conditions for the quartz, processing methods that eliminate residue from the substrate surfaces, high-density catalyst stripes formed from evaporated submonolayer films of iron, ethanol for the feed gas, and well-controlled temperature of the substrate. These procedures yield arrays of SWNTs with levels of perfection that are orders of magnitude better than previously reported results^{23–26} with coverages that are also substantially higher. Figure 1a–c shows scanning electron microscope (SEM) images of representative aligned arrays of SWNTs grown using these optimized approaches. The substrate was an ST-cut single-crystal quartz wafer,³¹ annealed in air at 900 °C for 8 h prior to growth. Isolated lines of catalyst on quartz were prepared by photolithographically patterning iron deposited by physical vapor deposition. In particular, the catalyst consisted of an ultrathin film (0.1–0.2 nm) of Fe uniformly deposited by electron beam evaporation (Temescal BJD1800) onto a photolithographically patterned layer of photoresist (AZ5214) on the quartz. After removing the photoresist with acetone and stripper (AZ Kwik stripper), samples were annealed at 900 °C for 1.5 h to form isolated iron oxide nanoparticles. The widths and spacings of the stripes patterned by photolithography that defined the spatial extent of these nanoparticles were 10 and 100 μm , respectively. The CVD process began by flushing the chamber with a high flow rate of Ar (3000 sccm) for 2 min and then heating the furnace to 925 °C while flowing H₂ (300 sccm). After stabilizing the temperature, flows of both H₂ and Ar were set to 8 sccm. Growth of SWNTs occurred by passing these gases through an ethanol bubbler held at 0 °C in a water bath chiller prior to entry into the chamber. Growth was terminated after 20 min, and the chamber was then cooled in H₂ and Ar flow. We estimate the growth rate of aligned SWNT formed in this manner to be between 0.5 and 2.5 $\mu\text{m}/\text{sec}$, consistent with previous reports for unaligned SWNTs grown by CVD on amorphous substrates.^{32,33}

As shown in Figure 1a,b, the degree of alignment and linearity in the SWNT arrays can be extremely high. In particular, the

percentage alignment, as measured using the total summed lengths of SWNT segments oriented along the preferred growth direction and of those oriented along any other direction, is reproducibly $>99.9\%$. The degree of linearity is also exceptionally high. For a typical tube shown in Figure 1c, for example, the maximum spatial deviation from a perfectly linear shape is ~ 5 nm along lengths of ~ 5 μm . This level of deviation is comparable to the uncertainty in determining the location of a tube by fitting the convolved height profile obtained with our atomic force microscope (AFM; DimensionV, Digital Ins.) equipped with a standard tip (radius of curvature ~ 20 nm). Figure 1d shows an AFM image of catalyst particles formed from 0.2 nm evaporated iron film. On the basis of AFM measurements in the regions of the catalyst, the average size of the iron oxide nanoparticles is 1.8 nm, as indicated in the histogram of Figure 1. Figure 1e presents the distribution of tube diameters, evaluated by AFM. The mean (~ 1.2 nm) and the range of diameters (0.4–4 nm) are similar compared to SWNTs grown using conventional CVD approaches. The degree of alignment and linearity do not depend on diameter for this range. The average densities of the arrays can be as high as 5–10 SWNT/ μm . Figure 2a shows an AFM image of aligned SWNTs with average tube density around 10 SWNT/ μm . At some areas, the tube density could be as high as 50 SWNT/ μm . Figure 2b shows an AFM image of SWNTs separated by a distance of ~ 15 nm. These results suggest that uniform densities at this level and perhaps higher are possible with suitable optimization. Increasing the thickness of the Fe catalyst film, the flow rate of the ethanol and other procedures designed to increase the density further typically lead to the formation of bundles and growth vertically out of the plane of the substrate in the regions of the catalyst. Further work and perhaps different strategies will be required to improve the densities to values substantially higher than those introduced here.

The separation distance between the lines of catalyst limits the lengths of the SWNTs in the arrays of Figure 1. Growth from an isolated catalyst line reveals the length distribution when the growth is not limited by structures on the substrate. Figure 3 shows some results. The average length is ~ 300 μm with

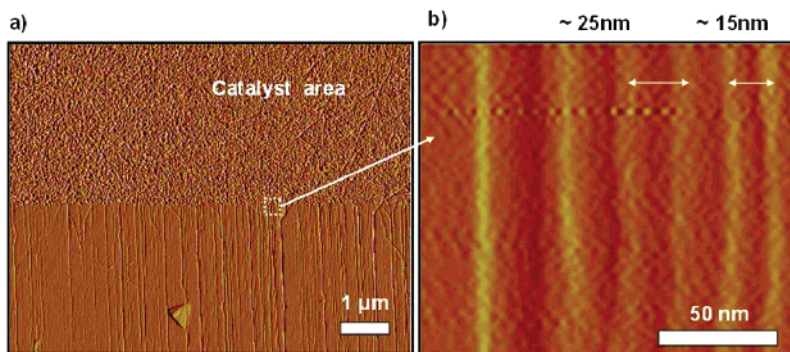


Figure 2. (a) AFM image of a dense array of SWCNTs emerging from a region of patterned catalyst. (b) High-resolution AFM image of a high-density region in this array. The shortest distance between two SWCNT, as measured in this fashion, is ~ 15 nm. In this area, the local tube density can be as high as 40–50 SWCNT/ μm .

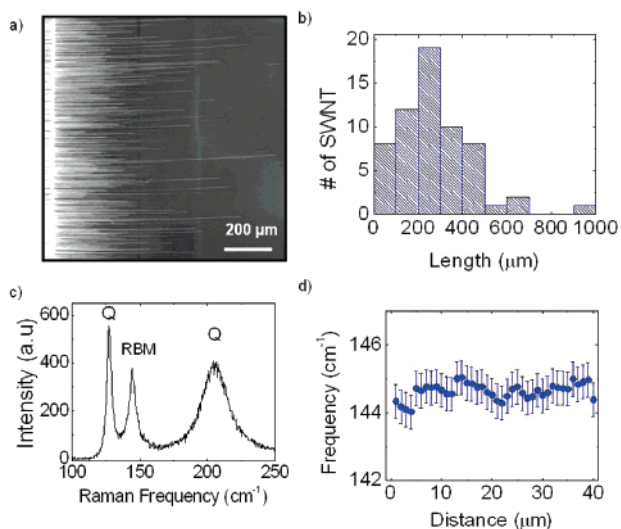


Figure 3. (a) Scanning electron microscope image of SWCNTs grown from a patterned line of Fe catalyst (vertical, bright stripe on the left side of this image). (b) Histogram of the lengths of SWCNTs shown in (a). The longest tube is ~ 1 mm, and the average length is ~ 300 μm . (c) Raman spectrum of an individual SWCNT from the array shown in (a), collected using a confocal spectrometer. The peaks labeled “Q” at ~ 127 and ~ 205 cm^{-1} are associated with the quartz substrate. The RBM of the SWCNT is at ~ 144.5 cm^{-1} . (d) Frequency of the RBM of a SWCNT as a function of position along its length. The frequency is constant to within the uncertainty of the measurement (± 0.5 cm^{-1}) for this 40 μm long segment.

some tubes that are as long as 1 mm. We observed that several factors influence the length. First, photoresist residue and high flow rates result in amorphous carbon formation and the early termination of growth. Second, growth temperatures (925–930 $^{\circ}\text{C}$) that are somewhat higher than those reported previously improve substantially the yield (i.e., the density) as well as the lengths. Third, cooling the ethanol bubbler (0 $^{\circ}\text{C}$) reduces the vapor pressure of ethanol and allows improved control over its concentration in the chamber thereby enabling the prevention of amorphous carbon formation.

There are a couple of mechanisms for growth termination. Depending on tip- or base-growth, the termination mechanism could be different. The growth mechanism with Fe catalyst on quartz is not known clearly. If we assume that it is base-growth, SWCNT must overcome the van der Waals forces between the tube and substrate to increase their length. When tubes reach a critical length, the driving force of the growth cannot overcome the van der Waals forces, and as a result growth will be terminated. Interestingly most of the tubes stop growing around the same length (~ 200 – 300 μm). If we assume the growth is

tip-growth, the termination mechanism should be related with the activation of the catalyst particles. Amorphous carbon formation on the catalyst can stop the growth. The life time of the active catalyst determines the length of the tube.

The long lengths and the relatively large separations between the ends of long tubes like those in Figure 3 allow Raman spectroscopy to be performed on individual aligned tubes in the array. Such information can provide valuable insights into the uniformity of the dimensions and chirality of a single tube along its length. The measurements used a confocal instrument (Jobin–Yvon) and a 100X microscope objective to focus the excitation laser (He–Ne, 632 nm wavelength; ~ 1 μm spot size; 5×10^5 W/cm^2 power density). The backscattered Raman signal was collected through a 50 μm pinhole. Figure 3c shows the results of a single point measurement on a typical SWCNT. The two Raman peaks around 127 and 205 cm^{-1} are due to quartz. The peak at 144 cm^{-1} is the radial breathing mode (RBM) of the SWCNT, which is related to the diameter of the tube. Figure 3d presents the frequency of the RBM as a function of position along the length of this tube. The results indicate a position independent value of 144 ± 0.5 cm^{-1} for the 50 μm length examined here. The variation in frequency is within the spectral resolution of the spectrometer (~ 0.5 cm^{-1}). These data suggest that the diameter (~ 1.7 nm) of the tubes in the arrays for the cases that we examined does not change during the growth process, which is consistent also with AFM measurements.

Isolated lines of catalyst provide SWCNT layouts convenient for studies such as those described above. The ability to define the locations and spatial layouts of the catalyst sites into other geometries can be important for applications that require unusual arrangements of aligned tubes or the integration of these aligned tubes with random networks of tubes. Figure 4 shows SEM images of some representative examples, including “wavy” line patterns (Figure 4a), arrays of disks (Figure 4b), and complex circuitlike structures (Figure 4c). The bright white regions correspond to high-coverage random networks of SWCNTs that grow in the areas where the catalyst is present. These networks have densities of ~ 100 SWCNT/ μm and sheet resistances of ~ 250 Ω/sq , suitable for use as transparent, tube-based interconnects between the aligned arrays of SWCNTs. The results of Figure 4b,c also illustrate clearly that the direction of gas flow is unimportant in determining the alignment in this process; aligned tubes grow equally well in directions that are different by 180 degrees.

The degree of alignment depends on the surface quality and cleanness of the quartz surface. Contamination or coatings on the surface affects the alignment. To illustrate this effect, we

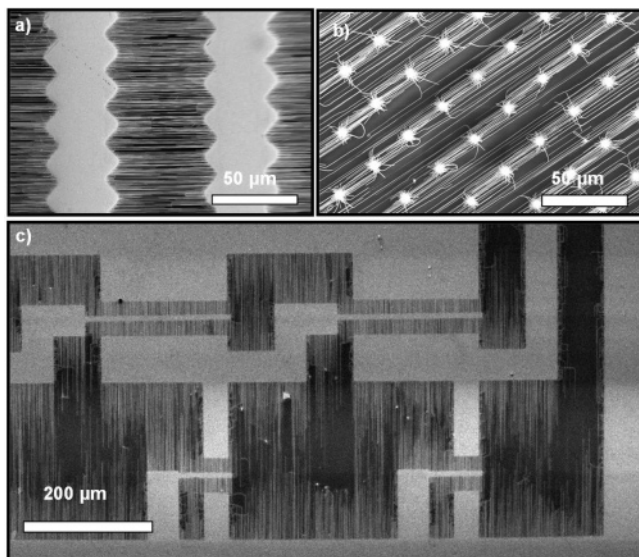


Figure 4. Aligned arrays of SWNT grown from catalysts particles patterned into different geometries, including (a) wavy lines, (b) circles ($2\ \mu\text{m}$ diameters separated by $25\ \mu\text{m}$), and (c) a complex circuit-like pattern.

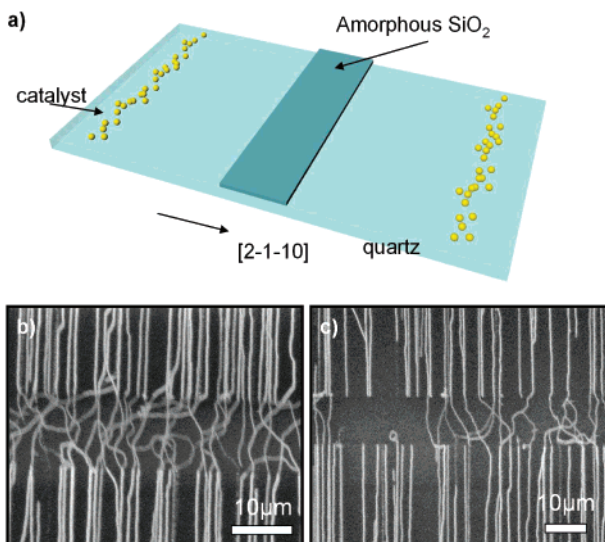


Figure 5. (a) Schematic illustration of the geometry of quartz with a $2\ \text{nm}$ thick patterned stripe of amorphous SiO_2 . (b, c) SEM images of SWNTs grown on this substrate.

grew SWNT on quartz with a patterned layer of amorphous SiO_2 ($\sim 2\ \text{nm}$ thickness) deposited by electron beam evaporation. Figure 5 shows schematic illustrations of this system, together with SEM views of SWNTs grown on this type of substrate. Aligned SWNTs that enter the SiO_2 -coated area lose alignment and grow in random directions. The SWNTs regain their alignment after emerging on the other side of the uncoated area. Some of the SWNTs (Figure 5c) stop at the interface of the SiO_2 pattern perhaps because of the small surface relief associated with this layer. These observations suggest that the SWNTs grow while in intimate contact with the quartz, which is quite different than the growth mechanisms typically observed on amorphous substrates.

In general, we do not observe effects of gas flow on SWNT alignment. Nevertheless, in rare instances near the edge of the sample, gas flow can be important perhaps because of high peak flow rates associated with turbulence in these regions. In these cases, interplay between gas flow and quartz-induced alignment occurs. When the SWNT touches the quartz surface, it orients

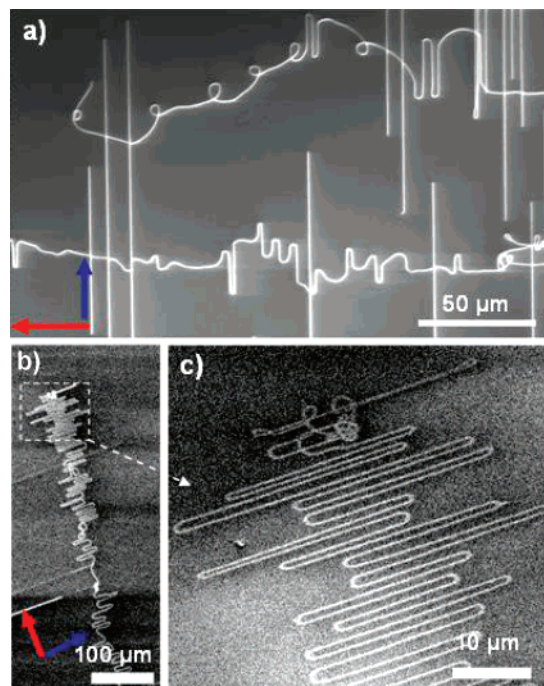


Figure 6. (a) SEM image of an SWNT formed into an unusual shape due to the combined effects of alignment due to the quartz surface (blue arrow indicates X -axis) and to gas flow (red arrow direction). (b) Large area and (c) zoomed SEM image of a zigzag shaped SWNT.

along the $[2-1-10]$ direction. Figure 6a shows different configurations of the SWNTs on the quartz surface. The SWNT along the blue arrow (X -axis) is aligned due to SWNT–lattice interaction, and the SWNT along the red arrow (indicating the flow direction) is aligned because of gas flow. The result is an unusual zigzag shape (Figure 6b,c).

Studies of SWNT growth on quartz substrates with different cuts can provide additional insights into the alignment mechanisms. Quartz crystal has a hexagonal crystal structure, which belongs to the rhombohedral crystal system. The alignment direction $[2-1-10]$ is known as the main axis (X -axis) of quartz. The basal plane (0001), has 3-fold symmetry. We examined growth on three different quartz surfaces: Y -cut (0010), Z -cut (0001), and X -cut ($2-1-10$), each of which has a different orientation with respect to the alignment axis. Figure 7a–c shows top views of a space-filling model of Y -cut (0010), Z -cut (0001), and X -cut ($2-1-10$) quartz, respectively. Figure 7d–f shows the orientation with respect to the main crystal axis. Scanning electron micrographs of SWNTs grown on these wafers are shown in Figure 7g–i. On Y -cut substrates, we observed alignment of SWNTs along the X -axis (Figure 7g), consistent with other results presented here and previously. On Z -cut wafers, which have 3-fold symmetry, we observed three alignment directions along three identical X -axes (Figure 7h). On the other hand, on the X -cut wafer we did not observe any alignment (Figure 7i). These observations indicate that SWNT prefer the $[2-1-10]$ direction. Strong anisotropic interaction is likely due to the arrangement of Si and O atoms. It is important to note that the piezoelectric effect in quartz is also observed along the X -axis.

One area of application for arrays such as these is in electronics. To explore these possibilities, we fabricated top-gated transistors that use the aligned SWNT arrays for the semiconducting channel, using recently reported procedures³⁴ but with different materials for the gate dielectrics, as discussed subsequently. For the device examples in Figure 5, the fabrica-

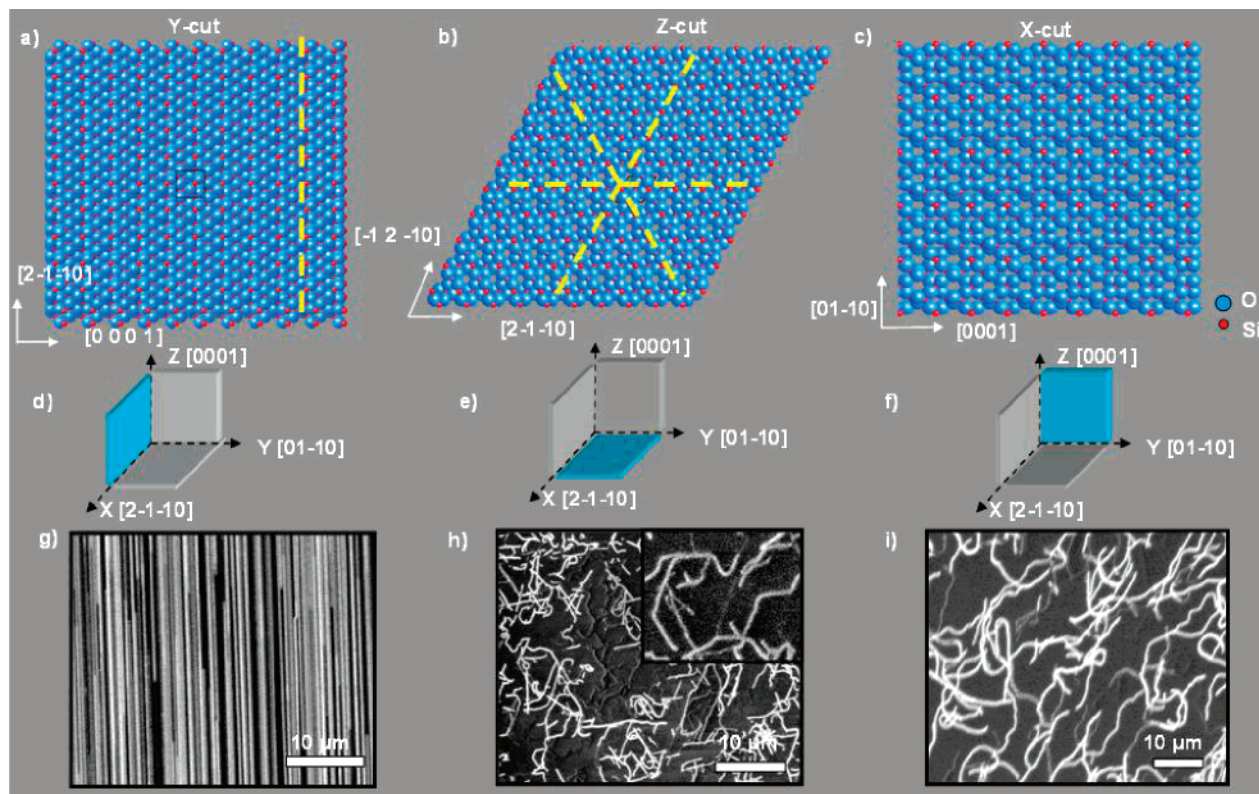


Figure 7. Space-filling model of Y-cut (a), Z-cut (b), and X-cut (c) quartz surfaces. (d–f) The insets show the orientation of the quartz surface with respect to main axis of quartz. SEM images of SWNTs grown on Y, Z, and X-cut quartz wafers, respectively. The Y-cut provides high degree of alignment along $[2-1-10]$ direction; Z-cut provides 3-fold symmetric alignment (inset in e shows a high-magnification SEM image); and X-cut does not provide any alignment.

tion began with the growth of aligned SWNTs using $10 \mu\text{m}$ wide catalyst lines separated by $100 \mu\text{m}$. Photolithography (AZ 5124) followed by uniform electron beam evaporation of Ti (1 nm), Pd (25 nm), and removal of the resist defined source and drain electrodes with gaps placed at parts of the substrates that do not include the patterned catalyst lines. After another photolithography step to protect the region between these electrodes, O_2 reactive ion etching (200 mTorr, 100 W) removed all of the exposed SWNTs to yield electrically isolated the devices. A hydrogen silsesquioxane (HSQ, Fox-12; Dow Corning) formed the gate dielectric. Spin coating (6000 rpm, 30 s) a precursor to this material and then baking (220°C for 10 min) created a uniform, 80 nm thick nanoporous layer. An advantage of HSQ is its excellent ability to conform to and planarize the underlying topography associated with the tubes and the source and drain electrodes. Even very thin (~ 30 nm) layers could be used effectively. The gate electrode (Ti, 1 nm; Au, 25 nm) was defined on top of the HSQ by photolithography and liftoff. Figure 8a gives a schematic illustration of a device. Figure 8b shows the atomic structure of the silsesquioxane and its integration with a SWNT. Imaging by SEM before depositing the gate dielectric and gate reveals the layout of the channel region of the device, as illustrated in Figure 8c. The variation in source/drain current (I_d) as a function of gate voltage (V_g) at a source/drain bias (V_d) of 0.5 V appears in Figure 8d for a device with 5 and $200 \mu\text{m}$ channel length (L_c) and width (W), respectively. The density of the array is ~ 5 SWNT/ μm . This device then involves the parallel operation of ~ 1000 individual SWNTs. The large output currents (i.e., mA) are consistent with this device design. The moderate ratio of currents in the on and off states results from the large numbers (~ 300) of metallic tubes that span the source and drain electrodes. The hysteresis observed in Figure 8d is characteristic of nanotube devices that

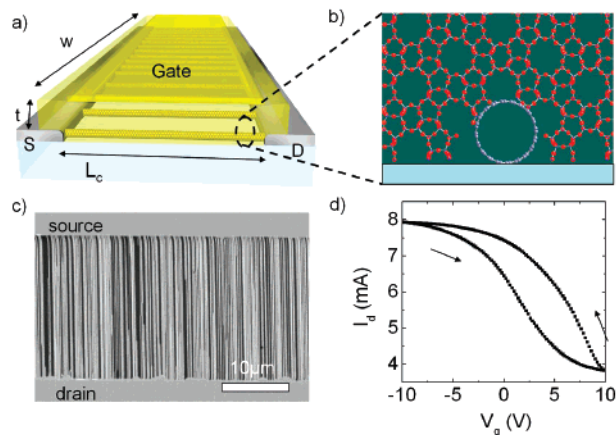


Figure 8. (a) Schematic illustration of the geometry of a thin film type transistor that uses aligned SWNTs as the semiconducting channel. (b) Atomic structure of a silsesquioxane gate dielectric coating a SWNT on a substrate. (c) SEM image of the channel region of a device like the one illustrated in (a). The bright regions at the top and bottom of this image are the source and drain electrodes. (d) Source/drain current (I_d) as a function of gate voltage (V_g) at a source/drain bias of 1 V. The arrows indicate the sweeping direction of the gate voltage.

operate at gate voltages larger than ~ 5 V. The hysteresis with the HSQ material, notably, is smaller at comparable gate fields than that observed with other materials. The reason for low hysteresis could be related to the porosity of HSQ materials and high-curing temperature (220°C). The detailed mechanisms for hysteresis in nanotube devices have been studied by other groups³⁵ and remain a topic of current research.

Figure 9 shows additional data from devices of this type. In particular, Figure 9a,b shows the scaling of device properties with channel length (L_c). As expected, both the on and off

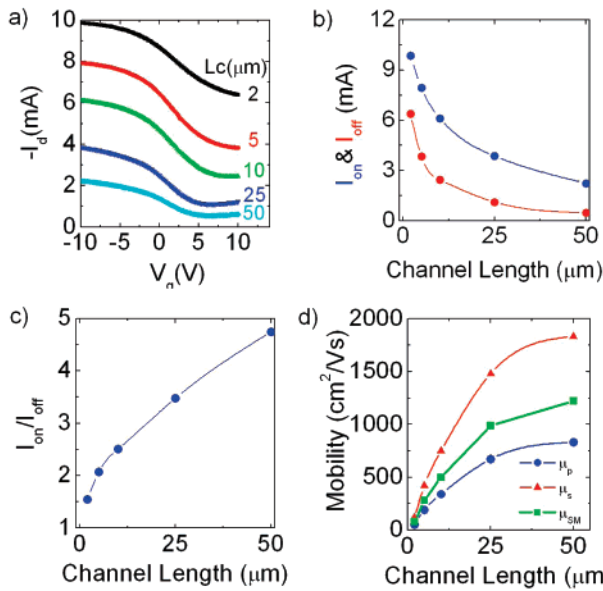


Figure 9. (a) Source/drain current (I_d) as function of gate voltage (V_g) at a source/drain bias of 1 V measured from thin film transistors that use SWNT arrays with channel widths of 200 μm and channel lengths (L_c) between 2 and 50 μm . (b) On current and off current (I_{on} and I_{off} , respectively) as a function of channel length. (c) Channel length dependence of on/off ratio. (d) Apparent mobility calculated using a parallel plate model for the capacitance (μ_p) and rigorous calculations of the device capacitance taking into account only semiconducting tubes (μ_s) and both metallic and semiconducting tubes (μ_{SM}).

currents (I_{on} and I_{off} , respectively) increase with decreasing channel length. The rate of increase is slightly less, however, than a $1/L_c$ scaling, likely due to the increasing relative role of contacts with decreasing L_c .

The linear regime mobilities can be calculated in several different ways. We define the effective field-effect mobility of the TFT device as

$$\mu_d = \frac{L_c}{V_d C W} \cdot \frac{dI}{dV_g} \quad (1)$$

where C is the capacitance per unit area. The simplest method approximates C as that of a uniform parallel plate capacitor. This estimate has been used in the past in thin film type SWNT devices,^{36,37} but it is valid only when the average spacing between adjacent tubes is significantly smaller than the thickness of the gate dielectric. Figure 9d shows the results of such calculations. We refer to this quantity as the thin film or device mobility.³⁴ (Since the effects of contacts are ignored completely in the above expression, the apparent mobility decreases with decreasing channel length.) A more rigorous definition of the mobility relies on explicit calculation of the capacitance coupling between the gate and the array of tubes, including the effects of fringing fields and electrostatic screening. The capacitance can be derived analytically for a uniformly spaced array of SWNTs by a variety of methods.^{34,36} An approach that uses classical electrostatics with image charge techniques and is applied to the case that the dielectric constant of the gate dielectric is similar to that of the substrate (geometry in Figure 8) yields the following expression for the total capacitance per unit area of the SWNT array:^{34,36}

$$C_{\text{tot}} = \frac{Q}{V} = \frac{N\rho}{V} \frac{2\pi\epsilon_0\epsilon_r N}{\ln\left(\frac{\sinh(\pi(2t+r)/\Delta L)}{\sinh(\pi r/\Delta L)}\right)} \quad (2)$$

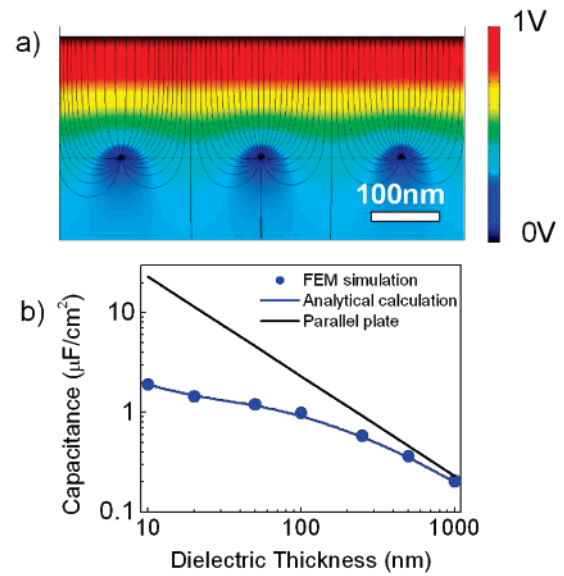


Figure 10. (a) Potential distribution associated with electrostatic coupling of a planar electrode to an array of SWNTs calculated by finite element modeling. The distance between the tubes is assumed to be constant. The Y -axis is scaled by 2. (b) Calculated capacitance for arrays with a tube density of 5 SWNT/ μm .

where Q is the total charge per unit area of the array, ρ is the linear charge density along a single SWNT in the array, V is the potential difference between a SWNT in the array and the gate electrode, N is the total number of tubes per unit length, ΔL is the distance between the tubes ($\Delta L = 1/N$) in the array, t is the gate dielectric thickness, ϵ_0 is the permittivity of free space, ϵ_r is the dielectric constant of the gate dielectric, and r is the tube diameter. In the limiting cases of low and high densities, eq 2 yields expressions consistent with a parallel plate ($C_p = \lim_{\Delta L \rightarrow 0} C_{\text{tot}} = \epsilon\epsilon_0/t$) and with a single tube ($C_s = \lim_{\Delta L \rightarrow \infty} C_{\text{tot}}/N = 2\pi\epsilon_0\epsilon_r/\ln((2t+r)/r)$), respectively, consistent with other reports.^{34,36,37} The metallic SWNTs in the array contribute to the device capacitance, but these tubes cannot be modulated with the gate field. The metallic tube capacitance represents a type of intrinsic parasitic capacitance, which can be modulated only by eliminating the metallic tubes and not, for example, by optimizing the device layout. For mobility calculation, we consider two different cases. In the first, because only semiconducting tubes can be modulated by the gate, we include only the capacitance of the semiconducting tubes ($C = N_s \cdot \rho/V$, where N_s is the number of semiconducting tubes per unit length). The mobility calculated with eq 1 and this rigorous value of the device capacitance yield a value that is equal to the average single tube mobility. In the second case, we include capacitance contributions from both the metallic and the semiconducting tubes, such that the mobility is equal to two thirds of single tube mobility. Figure 9d shows scaling of the calculated mobility using different capacitance value. The per tube mobilities ($\sim 2000 \text{ cm}^2/\text{Vs}$) of the semiconducting SWNT inferred from these measurements are in the same range as independent measurements on devices that incorporate individual tubes.¹⁷ Finite element modeling (FEM) reproduces these limits as well as the functional variations between them. Figure 9d shows the results of mobilities computed with eq 1. The values are systematically higher than those estimated with the parallel plate model, as expected. Figure 10a shows the calculated field distribution and electric-field lines using eq 2. Figure 10b presents the calculated capacitance as a function of dielectric thickness, derived with eq 2 and FEM simulation.

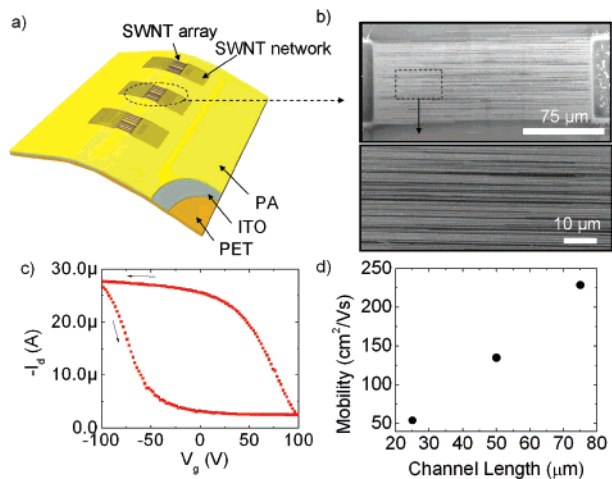


Figure 11. (a) Schematic geometry of a TFT on an ITO-coated PET substrate. (b) SEM images of TFTs that use aligned arrays of SWNT as the semiconductor and dense SWNT networks as source and drain electrodes. (c) Source/drain current (I_d) as function of gate voltage (V_g) at a source/drain bias of 0.5 V of the TFT as a function of gate voltage. (d) Channel length dependence of calculated field effect mobility calculated using parallel plate capacitance.

In addition to devices such as these that use SWNTs for the channel, it is possible to combine random networks with aligned arrays to produce all-tube devices. Such designs can yield optically transparent devices with the ability for integration on flexible plastic substrates for possible applications in flexible heads-up displays and other systems. This type of nanotube approach to transparent thin film transistors could complement recently reported strategies that use inorganic semiconducting and conducting oxides,³⁸ organic transistors with networks of SWNT as electrodes,³⁹ and transistors that use networks of SWNTs for both the semiconductor and electrodes.⁴⁰ The fabrication for devices presented here began with the patterning of thin (<0.5 nm) Fe catalyst into shapes that define the source and drain electrodes on a quartz substrate. The optimized CVD techniques described previously yielded collections of SWNTs in layouts, qualitatively similar to those shown in Figure 4, from these catalyst patterns. Dense, random networks and aligned arrays of SWNTs formed in the areas coated and uncoated with catalyst, respectively. Aligned SWNTs that emerge from the catalyst areas grow along the preferred direction on the quartz to connect two random networks. Figure 11a,b shows schematic illustration of final device and SEM images of networks and arrays. Transfer printing^{39,41} these structures onto thin plastic substrates (PET) coated with layers of indium tin oxide (100 nm; ITO) as the gate electrode and Polyamide (1 μm, polyamic acid, Aldrich) as the gate dielectric formed the final device. The dense random networks of SWNTs serve as the source and drain electrodes. Probing these devices by physically contacting the source, drain, and gate electrodes using conventional probe tips reveals their electrical properties (Figure 11c,d). These devices show mobilities as high as ~240 cm²/Vs, computed using the parallel plate models for C. The large hysteresis is characteristic of high-operation voltages and thick dielectrics. The relatively high sheet resistances (~250 Ω/sq) of the source and drain electrodes contribute to device resistance and reductions in apparent mobility with channel length.

In summary, this paper demonstrates an optimized, reliable CVD process capable of producing large scale arrays of SWNTs that offer levels of perfection in alignment and linearity that are orders of magnitude better than previously reported results. Thin film transistors that use these arrays show device level

performance that approaches values expected based on the intrinsic properties of the SWNTs with good device-to-device uniformity. The array geometry greatly simplifies the integration of SWNT into complex circuits for a range of other applications such as light-emitting diodes, photodetectors, chemical sensors, nanoelectromechanical oscillators, and electrically or thermally conductive elements.

Acknowledgment. We thank T. Banks and K. Colravy for help with processing using the facilities at the Frederick Seitz Materials Research Laboratory. This material is based upon work supported by the National Science Foundation under Grant NIRT-0403489 and the U.S. Department of Energy, Division of Materials Sciences under Award No. DEFG02-91ER45439, through the Frederick Seitz MRL and Center for Microanalysis of Materials at the University of Illinois at Urbana-Champaign.

References and Notes

- (1) Ahn J. -H.; Kim H. -S.; Lee K. J.; Zhu Z.; Menard E.; Nuzzo R. G.; Rogers, J. A. *IEEE Electron Device Lett.* **2006**, *27*, 460.
- (2) Ahn, J. -H.; Kim, H. -S.; Lee, K. J.; Jeon, S.; Kang, S. J.; Sun, Y.; Nuzzo, R. G.; Rogers J. A. *Science* **2006**, *314*, 1754.
- (3) Wu, Y.; Cui, Y.; Huynh, L.; Barrelet, C. J. D.; Bell, C.; Lieber, C. M. *Nano Lett.* **2004**, *4*, 433.
- (4) Kong, J.; Franklin, N. R.; Zhou, C.; Chapline, M. G.; Peng, S.; Cho, K.; Dai, H. *Science* **2000**, *284*, 622.
- (5) Star, A.; Gabriel, J. P.; Bradley, K.; Grüner, G. *Nano Lett.* **2003**, *3* (4), 459.
- (6) Snow, E. S.; Perkins, F. K.; Houser, E. J.; Badescu, S. C.; Reinecke, T. L. *Science* **2005**, *307*, 1942.
- (7) Chen, J.; Perebeinos, V.; Freitag, M.; Tsang, J.; Fu, Q.; Liu, J.; Avouris, P. *Science* **2005**, *310*, 1171.
- (8) Wu, Z.; Chen, Z.; Du, X.; Logan, J. M.; Sippel, J.; Nikolou, M.; Kamaras, K.; Reynolds, J. R.; Tanner, D. B.; Hebard, A. F.; Rinzler, A. G. *Science* **2004**, *305*, 1273.
- (9) Zhou, Y. X.; Gaur, A.; Hur, S. H.; Kocabas, C.; Meitl, M. A.; Shim, M.; Rogers, J. A. *Nano Lett.* **2004**, *4*, 2031.
- (10) Snow, E. S.; Novak, J. P.; Campbell, P. M.; Park, D. *Appl. Phys. Lett.* **2003**, *82*, 2145.
- (11) Artukovic, E.; Kaempgen, M.; Hecht, D. S.; Roth, S.; Grüner, G. *Nano Lett.* **2005**, *5*, 757.
- (12) Hu, L.; Hecht, D. S.; Grüner, G. *Nano Lett.* **2004**, *4*, 2513.
- (13) Kumar, S.; Pimparkar, N.; Murthy, J. Y.; Alam, M. A. *Appl. Phys. Lett.* **2006**, *88*, 143501.
- (14) Javey, A.; Guo, J.; Wang, Q.; Lundstrom, M.; Dai, H. *Nature* **2003**, *4* (24), 654.
- (15) Bosnick, K.; Gabor, N.; McEuen, P. L. *Appl. Phys. Lett.* **2006**, *89*, 163121.
- (16) Alam, M. A.; Pimparkar, N.; Kumar, S.; Murthy, J. *MRS Bull.* **2006**, *31*, 466.
- (17) Zhou, X.; Park, J.-Y.; Huang, S.; Liu, J.; Mceuen, P. L. *Phys. Rev. Lett.* **2005**, *95*, 146805.
- (18) Durkop, T.; Getty, S. A.; Cobas, E.; Fuhrer, M. S. *Nano Lett.* **2004**, *4*, 35.
- (19) Yao, Z.; Kane, C. L.; Dekker, C. *Phys. Rev. Lett.* **2000**, *84*, 2941.
- (20) Lin, Y.-M.; Appenzeller, J.; Knoch, J.; Avouris P. *IEEE Trans. Nano.* **2005**, *4*, 481.
- (21) Snow, E. S.; Campbell, P. M.; Ancona, M. G.; Novak, J. P. *Appl. Phys. Lett.* **2005**, *86*, 033105.
- (22) Hur, S. H.; Kocabas, C.; Gaur, A.; Park, O. O.; Shim, M.; Rogers, J. A. *J. Appl. Phys.* **2005**, *98*, 114302.
- (23) Kocabas, C.; Hur, S. H.; Gaur, A.; Meitl, M. A.; Shim, M.; Rogers, J. A. *Small* **2005**, *1*, 1110.
- (24) Kocabas, C.; Shim, M.; Rogers, J. A. *J. Am. Chem. Soc.* **2006**, *128*, 4540.
- (25) Ismach, A.; Segev, L.; Wachtel, E.; Joselevich, E. *Angew. Chem., Int. Ed.* **2004**, *43*, 6140.
- (26) Han, S.; Liu, X. L.; Zhou, C. W. *J. Am. Chem. Soc.* **2005**, *127*, 5294.
- (27) Kumar, S.; Murthy, J. Y.; Alam, M. A. *Phys. Rev. Lett.* **2005**, *95*, 0668021.
- (28) Pimparkar, N.; Guo, J.; Alam, M. A. *Tech. Dig. - Int. Electron Devices Meet.* **2005**, *21.5*, 541.
- (29) Fuhrer, S.; Nygård, J.; Shih, L.; Forero, M.; Yoon, Y.-G.; Mazzone, M. S. C.; Choi, H. J.; Ihm, J.; Louie, S. G.; Zettl, A.; McEuen, P. L. *Science* **2000**, *288*, 494.
- (30) Ismach, A.; Kantorovich, D.; Joselevich, E. *J. Am. Chem. Soc.* **2005**, *127*, 11554.

- (31) Hoffman Mat. Inc.
- (32) Huang, S.; Maynor, B.; Cai, X.; Liu, J. *Adv. Mat.* **2003**, *15*, 1651.
- (33) Zheng, L. X.; O'Connell, M. J.; Doorn, S. K.; Liaon, X. Z.; Zhao, Y. H.; Akhadov, E. A.; Hoffbauer, M. A.; Roop, B. J.; Jia, Q. X.; Dye, R. C.; Peterson, D. E.; Huang, S.; Liu, M.; Zhu, J. Y. T. *Nat. Mater.* **2004**, *3*, 673.
- (34) Kang, S. J.; Kocabas, C.; Ozel, T.; Shim, M.; Pimparkar, N.; Alam, M. A.; Rotkin, S. V.; Rogers, J. A. *Nat. Nanotechnol.* **2007**, *2*, 230.
- (35) Kim, W.; Javey, A.; Vermesh, O.; Wang, Q.; Li, Y.; Dai, H. *Nano Lett.* **2003**, *3*, 193.
- (36) Cao, Q.; Xia, M.; Kocabas, C.; Shim, M.; Rogers, J. A.; Rotkin, S. V. *Appl. Phys. Lett.* **2007**, *90*, 023516.
- (37) Guo, J.; Goasguen, S.; Lundstrom, M.; Datta, S. *Appl. Phys. Lett.* **2002**, *81*, 1486.
- (38) Wang, L.; Yoon, M.-H.; Lu, G.; Yang, Y.; Facchetti, A.; Marks, T. J. *Nat. Mater.* **2006**, *5*, 893.
- (39) Cao, Q.; Zhu, Z. T.; Lemaitre, M. G.; Xia, M. G.; Shim, M.; Rogers, J. A. *Appl. Phys. Lett.* **2006**, *88*, 113511.
- (40) Cao, Q.; Hur, S.-H.; Zhu, Z.-T.; Sun, Y. G.; Wang, C.-J.; Meitl, M. A.; Shim, M.; Rogers, J. A. *Adv. Mater.* **2006**, *18*, 304.
- (41) Hur, S.-H.; Park, O. O.; Rogers, J. A. *Appl. Phys. Lett.* **2005**, *86*, 243502.